International Journal of Advanced Multidisciplinary Application | IJAMA
Volume 3 Issue 11 Nov 2026
ISSN No: 3048-9350

Green Synthesis, Structural Characterization, And In Vitro Anticancer Evaluation of *Azadirachta Indica*-, *Cinnamomum Verum*-, And *Ruta Graveolens*–Capped Zinc Oxide Nanoparticles Against Human Cervical Cancer (HeLa) Cells

Jai Thomas[1], Fibin Varghese T. V[2], Sanoop A. P[3]
[1,3] Assistant Professor, PG & Research Department of Chemistry, St. Mary's College, Sulthan Bathery, Kerala, India,
[2] Assistant Professor, PG & Research Department of Physics, St. Mary's College, Sulthan Bathery, Kerala, India
Email: [1]jaithomas1986@gmail.com, [2]fibinv@gmail.com,[3] sanoop.paulose@gmail.com

Abstract

Zinc oxide nanoparticles (ZnO NPs) were synthesized by a green chemical method utilising flora - Azadirachta indica (Neem, ZnN), Cinnamomum verum (Cinnamon, ZnK), and Ruta Graveolens (Common Rue, ZnS), alongside an uncapped control (ZnB), and were analysed using XRD, FESEM, FTIR, and BET techniques. XRD studies showed the production of pure wurtzite ZnO, with crystallite sizes ranging from 16.9 nm to 27.7 nm. FESEM analysis revealed that each sample had varied morphologies based on the capping agent used, demonstrating the impact of diverse capping agents in determining the morphology of zinc oxide samples. It also validates the findings of BET surface area measurements, which showed that ZnS was followed by ZnN, ZnK, and ZnB in order of increasing surface area. Anticancer studies on these samples showed that ZnS has the highest anticancer property followed by ZnN,ZnB and ZnK which showed the importance of different capping agents on the anticancer properties.

Keywords: ***Azadirachta indica*, *Cinnamomum verum*, *Ruta graveolens*, HeLa cells, cervical cancer, MTT assay, anticancer activity**

1. Introduction

Cancer remains one of the leading causes of morbidity and mortality worldwide, and conventional treatment modalities: chemotherapy, radiotherapy, and surgery continue to be limited by poor selectivity toward malignant cells and consequent systemic (Bisht & Rayamajhi, 2016). Therefore, there is continued interest in developing nanomedicines where nanoparticles are designed to utilize the enhanced permeation and retention (EPR) effect, tunable surface chemistry characteristics and/or intrinsic and selective cytotoxic effects of nanoparticles on cancerous cells(Davis et al., 2008).

One class of metal oxide nanoparticles being explored for use in cancer treatment include zinc oxide nanoparticles (ZnO NPs)(Hamad et al., 2025; Raha & Ahmaruzzaman, 2022). Zinc plays many important roles in mammalian physiology including acting as a co-factor for over 300 mammalian enzymes, participating in apoptosis, DNA repair and cell cycle regulation (Bisht & Rayamajhi, 2016)and thus makes ZnO NP's attractive candidates for treating cancer. It has been reported that the mechanism of cytotoxicity of ZnO NP's toward cancer cells involves both zinc ion mediated disruption of cellular enzyme function after intracellular dissolution of Zn^{2+} ions, production of reactive oxygen species (ROS) produced via photoinduced charge carrier recombination through the wide direct bandgap, 3.37 eV (Agarwal et al., 2017; Raha & Ahmaruzzaman, 2022)and large exciton binding energy. 60 meV of ZnO (Li et al., 2017), and preferential electrostatic interactions between the positively charged ZnO surface at physiological pH and the negatively charged phospholipid-rich membranes characteristic of cancer cells resulting in

localized delivery and toxicity of ZnO NP's that is significantly higher than noncancerous cells (Davis et al., 2008; Maher et al., 2023).

Green (biologically mediated) synthesis methods are advantageous in terms of cost-effectiveness [8] and the potential to produce nanoparticles with additional bioactivity imparted by phytochemicals bound to the nanoparticle surfaces [3], in addition to avoiding potentially hazardous chemicals used in traditional synthesis methods. Numerous plant-based ZnO NP caps have demonstrated concentration-dependent cytotoxicity against a range of cancer cell lines, including: For instance, ZnO NPs made from Sisymbrium irio showed up to 90% cytotoxicity (IC50 = 0.4769 mg/mL) against HepG2 and BHK cells [7], while ZnO NPs coated with β-cyclodextrin and Phyllanthus emblica emulsion showed a dose-dependent anticancer effect against KB-31 cells with little effect on normal Vero cells [9]. When taken as a whole, these investigations include a thorough analysis of the literature on ZnO production using plant extracts by Raha and Ahmaruzzaman (2022) indicate that the selection of capping phytochemical(s) greatly affects the physical properties of ZnO NP's including particle size, morphology, surface area and ultimately their biological activity (Raha & Ahmaruzzaman, 2022). Azadirachtin and nimbin in neem (Azadirachta indica), cinnamaldehyde and eugenol in cinnamon (Cinnamomum verum), and furanocoumarins and alkaloids in common rue (Ruta graveolens) are just a few of the traditionally used medicinal plants that have been shown to contain antioxidant, antimicrobial, and cytotoxic compounds [10], [11]. The effectiveness of ZnO NPs capped with each of these three plants in comparison to an uncapped control (blank) against HeLa human cervical cancer cells has not, however, been documented. We have created a new method to produce blank (ZnB), Neem (ZnN), Cinnamon (ZnK), and Rue-capped (ZnS) ZnO nanoparticles using the sol-gel method under the same conditions for evaluation based on a unified characterisation and cytotoxic assessment framework in response to this research need. Consequently, we will be able to link variations in structure and surface properties among ZnO NP formulations with their respective anticancer efficacies.

One of the most common types of cancer in women worldwide is cervical cancer, which is also one of the leading causes of cancer-related deaths in women [12], [13]. Many of these deaths, in particular, take place in low- and middle-income nations where access to HPV immunizations and screening programs may be limited [12]. The majority of cervical malignancies are caused by persistent infection with high-risk strains of the human papillomavirus (HPV), particularly HPV-16 and HPV-18, which cause malignant alterations in cervical epithelial cells [14]. Therefore, platinum-based chemotherapy, radiation therapy, and surgery are being used to treat cervical cancer. But, ongoing need for new, selective therapeutic agents for use in treating this type of cancer (Burmeister et al., 2022).

One of the most well researched, well-characterized, and often utilized models for in vitro investigations of human pharmacology and nanotoxicology is the HeLa cell line [15]. Its high growth rates, ease of culture, thorough characterisation, and accessibility are the factors contributing to its widespread application [16]. HeLa cells are a perfect starting point for testing potential anticancer medications and metal oxide nanoparticles because of all these qualities. Thus, using HeLa cells as a standard in vitro model system for human cervical cancer, this work evaluates the lethal characteristics of physiologically capped zinc oxide nanoparticles (ZnO NPs) [7], [17].

2. Materials and Methods

2.1 Materials

Zinc acetate dihydrate (≥99%, Sigma-Aldrich) was used as the zinc precursor. Sodium hydroxide (≥98%, Merck) was used as the precipitating agent. All solutions were prepared in deionised water. All chemicals were purchased from commercial suppliers and used without further purification

2.2 Plant Extract Preparation

The fresh leaves of *Azadirachta indica, Cinnamomum verum, Ruta graveolens* were collected, the leaves were thoroughly washed multiple time with deionized water to clean the surfaces, then allowed to air dry in the shade to preserve sensitive compounds such as volatile terpenoids and flavonoid. The dried material (approximately 20 grams per batch) was boiled with 100 mL of deionized water for one hour at 60^0C while being stirred continuously with a magnetic stirrer. The resultant filtrate, collected through Whatman No. 1 filter paper, served as the capping agent extract and was stored at 4°C until use.

2.3 Synthesis of ZnO nanoparticles (ZnB, ZnK, ZnN, ZnS)

Zinc acetate dihydrate solution (21.94 g in 50 mL) is stirred for 20 minutes at 60^0C to make it homogeneous. Cool this solution to 35^0C and add NaOH solution (4g in 50 mL) drop wise with vigorous stirring. Continue stirring for further 10 minutes and add the plant extract into this drop wise with constant stirring. For blank add deionise water. The white precipitate formed was $Zn(OH)_2$, filtered through Whatman filter paper, dried each samples overnight in an oven at 80^0C. After drying the samples are calcined at 200^0C for 4hours to get white ZnO powders. It was then undergone for characterizations and applications.

2.4 Characterization

Field Emission Scanning Electron Microscopy (FESEM) was used to examine particle morphology and degree of agglomeration for each sample. Brunauer–Emmett–Teller (BET) surface area, pore volume, and mean pore diameter were determined from nitrogen adsorption–desorption isotherms recorded at 77 K, following outgassing at 200 °C for 4 h. X-ray diffraction (XRD) was used to confirm the crystal phase and to estimate crystallite size via the Scherrer equation. Fourier-transform infrared (FTIR) spectroscopy was used to identify the characteristic Zn-O stretching vibration and capping-agent-derived surface functional groups.

2.5 In vitro cytotoxicity (MTT assay)

The HeLa (human cervical cancer) cell line was procured from the National Centre for Cell Sciences (NCCS), Pune, India, and maintained in Dulbecco's Modified Eagle Medium (DMEM, Sigma-Aldrich, USA) supplemented with 10% fetal bovine serum, L-glutamine, sodium bicarbonate (Merck, Germany), and an antibiotic solution (penicillin 100 U/mL, streptomycin 100 µg/mL, amphotericin B 2.5 µg/mL). Cultures were maintained at 37 °C in a humidified 5% CO_2 incubator (NBS Eppendorf, Germany).

For the assay, a two-day-old confluent monolayer was trypsinised and seeded at 5×10^3 cells/well (100 µL cell suspension in 10% growth medium) in 96-well tissue culture plates and incubated for 24 h at 37 °C, 5% CO_2. Each ZnO sample (ZnB, ZnK, ZnN, ZnS) was prepared as a 1 mg/mL stock in 0.1% DMSO and sterile-filtered (0.22 µm). After the initial 24 h incubation, the growth medium was replaced with freshly prepared sample solutions at 6.25, 12.5, 25, 50, and 100 µg/mL in DMEM (triplicate wells per concentration), alongside untreated control wells, and plates were incubated for a further 24 h. Cells were also examined by inverted phase-contrast microscopy (Olympus CKX41 with Optika Pro5 CCD camera) for morphological indicators of cytotoxicity (rounding, shrinkage, granulation, cytoplasmic vacuolisation).

For the colorimetric readout, MTT (Sigma, M-5655; 15 mg reconstituted in 3 mL PBS, filter-sterilised) was added (30 µL/well) after removal of the sample-containing medium, and plates were incubated for a further 4 h at 37 °C, 5% CO_2. The supernatant was then removed and 100 µL of DMSO (Sigma-Aldrich) was added per well to solubilise the formazan crystals. Absorbance was read at 540 nm on a microplate reader. Percentage cell viability was calculated as (mean OD of treated sample / mean OD of untreated control) × 100. IC50 values were determined from the resulting dose–response curves using ED50 PLUS v1.0 software.

3. Results and Discussion

3.1 X-ray diffraction (XRD) analysis

The X-ray diffraction patterns of the ZnO nanoparticles were recorded using a PANalytical X-ray diffractometer with Cu Kα radiation (λ = 1.5406 Å) at 40 kV and 15 mA over the 2θ range of 5°–80° at a step size of 0.0435° and counting time of 22.44 s per step. XRD patterns were recorded for all four samples, represented in figure 1. All major reflections for ZnB, ZnK, ZnN, and ZnS matched the standard hexagonal wurtzite ZnO pattern (JCPDS card no. 36-1451) namely the (100), (002), (101), (102), (110), (103), (112), and (201) planes confirming that the wurtzite phase was retained regardless of capping agent, and that no secondary/impurity phases were detected within the sensitivity of the measurement.

Peak positions were essentially unshifted across the series (e.g., the (101) reflection fell within 36.21–36.34° for all four samples), indicating that capping did not introduce measurable lattice strain or a change in unit-cell symmetry. Lattice parameters calculated from the (100) and (002) reflections ($a = 2d_{100}/\sqrt{3}$, $c = 2d_{002}$) gave $a \approx 3.24$–3.25 Å and $c \approx 5.19$–5.21 Å

for all samples (Table 4), in close agreement with literature values for bulk wurtzite ZnO (a = 3.2495 Å, c = 5.2069 Å), further confirming phase purity (Mani et al., 2023).

Using the Scherrer equation, D = Kλ/[(FWHM) × cos(θ)] where K = 0.9, the size of the crystalline material, D, has been calculated by measuring the peak broadening at half height (FWHM) for each sample [19]. The FWHM value has been calculated as an average over the clearly resolved planes and for the most intense and well-resolved (101) plane. The declining values of D are in the same order in both situations: ZnB (30.2 nm/27.7 nm average) > ZnK (27.5 nm/25.1 nm average) > ZnN (20.2 nm/18.0 nm average) > ZnS (19.1 nm/16.9 nm average). These findings demonstrate a distinct and unidirectional impact of the encapsulated agent on the particle size since the particle sizes in all samples treated with plant extract have decreased compared to the blank without capping, and among these, the extract from Ruta graveolens produces smaller particles than the other two extracts.

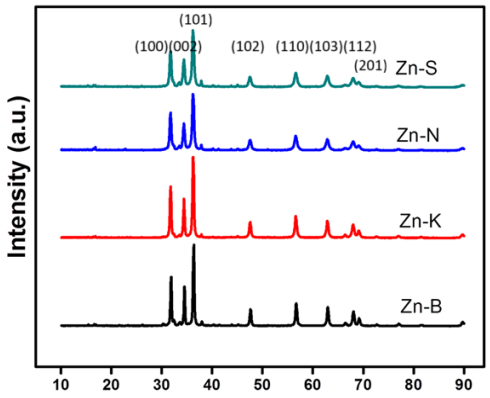


Figure 1: XRD diffraction patterns of the four samples ZnB, ZnK, ZnN and ZnS

3.2 Morphological analysis (FESEM)

The surface morphology, particle size, and size distribution of the synthesised ZnO nanoparticles were examined by field emission scanning electron microscopy (FESEM) using a ZEISS FESEM instrument equipped with an InLens secondary electron detector. All micrographs were acquired at an accelerating voltage (EHT) of 10.00 kV and a working distance (WD) of 4.6 mm using Signal A (InLens) detection mode. Images were recorded at magnifications ranging from 50,000× to 450,000× with a calibrated scale bar of 200 nm. The FESEM images of the four samples are depicted in figure 2, and its surface morphology is explained in Table 1. The particulate sample without a cap on it (ZnB) was characterized as having a combination of both rod-shaped and granule type material that had considerable agglomeration. These types of agglomerations are characteristic of un-stabilized ZnO that has precipitated out of solution without an organic layer present to stabilize the particles. When the cinnamon extract (ZnK) was introduced into this process, a significantly more fused and hierarchical surface structure was observed. Furthermore, there were significantly less clearly defined individual particles visible under magnification. This would suggest that the cinnamon phytoconstituents (cinnamaldehyde or eugenol derived phenolic compounds) have formed significant bridges between the growing ZnO particles thereby limiting their ability to form separate discrete crystallites (Davis et al., 2008). The neem capped sample (ZnN) appeared to exhibit both elongated rod-shaped crystallites along with cauliflower like clusters composed of finer granules. These characteristics suggest that neem extracts (azadirachtin and nimbin type phyto-chemicals) only partially restrict the growth and fusion of individual particles (Zambri et al., 2019). In contrast, the rutacarpine capped sample (ZnS) possessed the most distinct morphology within the entire set of samples analyzed. The rutacarpine capped sample consisted of large flower/urchin type structures made up of radiating subunits. The formation of such a unique and well-defined morphology suggests that rutacarpine (a furanocumarin/alkaloid derived compound found in *Ruta graveolens*), effectively caps and directs the growth of the ZnO crystallites, this unique morphology exhibited by the rutacarpine capped

ZnO is indicative of a larger surface area of the ZnS compared to the other three capped samples examined (Davis et al., 2008; Lingaraju et al., 2016).

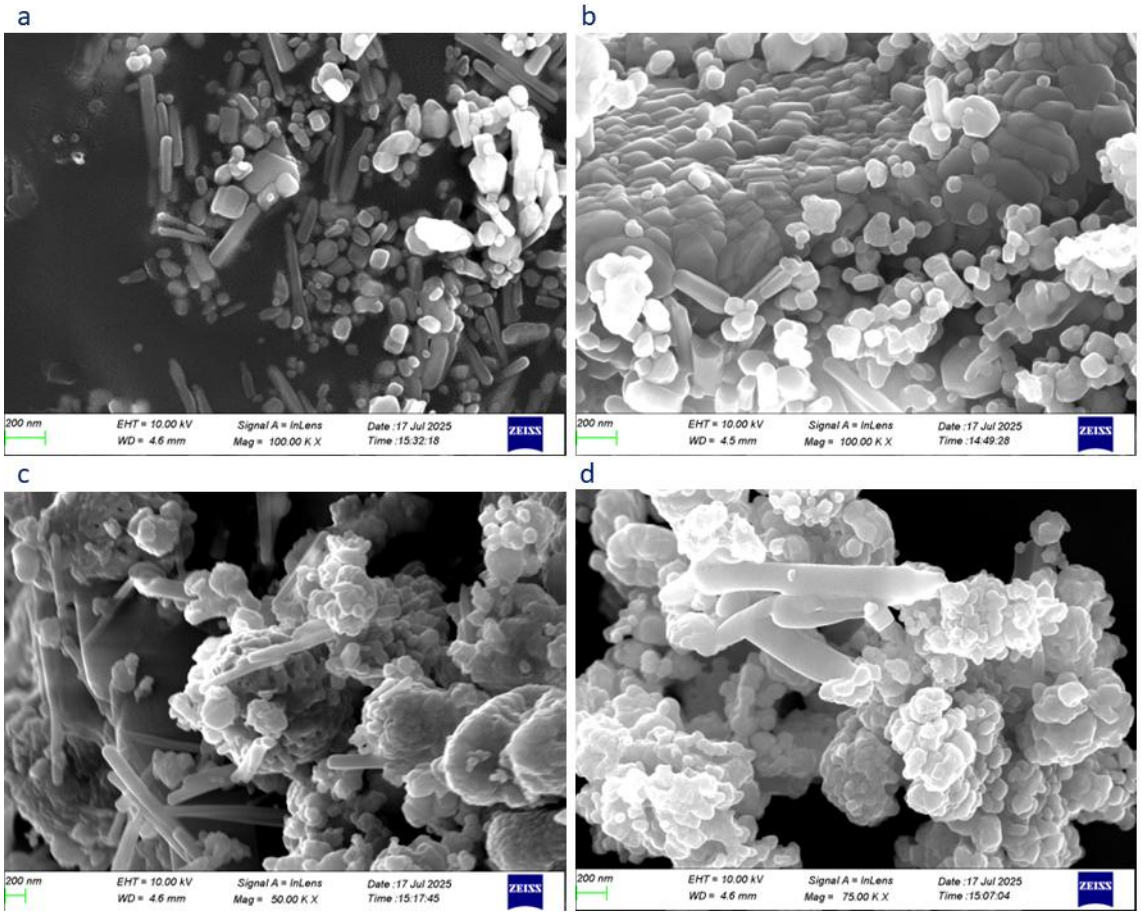


Figure 2: FESEM images (a) ZnB (b) ZnK (c) ZnN (d) ZnS

Table 1: Surface morphology description using FESEM

Sample	Representative morphology observed	Predominant features
ZnB	Mixed rod-/hexagonal-plate and granular particles, moderately agglomerated	Rod-like crystallites intergrown with granular aggregates; some isolated well-faceted particles
ZnK	Densely fused, hierarchical granular clusters with a corrugated surface	High degree of particle-particle fusion/agglomeration; fewer discrete particle boundaries than ZnB
ZnN	Cauliflower-like clusters of fine granules interspersed with elongated rods	Mixed rod and spherical granule morphology; clusters of sub-granules forming larger secondary particles
ZnS	Well-defined "urchin"-/flower-like spherical aggregates built from radiating sub-units, plus discrete rod bridges	Most distinctive morphology of the series; high apparent surface roughness consistent with its higher BET surface area

3.3 FTIR analysis

Fourier-transform infrared (FTIR) spectroscopy was performed using a PerkinElmer Spectrum IR spectrometer (Version 10.7.2) to identify the functional groups present in the synthesised ZnO nanoparticles and to confirm the presence of surface-bound phytochemical capping agents. Spectra were recorded in the wavenumber range of 4000–400 cm^{-1} in percentage

transmittance (%T) mode. All samples were prepared as KBr pellets using the standard KBr disc method, in which approximately 1–2 mg of sample was finely ground and mixed with 100–200 mg of spectroscopic-grade KBr, pressed into a transparent disc under hydraulic pressure, and immediately analysed. The reported spectra passed all instrument quality checks with no warnings flagged by the PerkinElmer Spectrum IR software. All spectra were collected in ATR mode and it confirms the characteristic features and chemical structure of ZnO NPs and are depicted in figure 3. Four spectral features were consistently resolved across all four samples: a weak C-H stretching band (~2960-3010 cm^{-1}), a broad, H-bonded O-H stretching envelope (~3050-3160 cm^{-1}), a dominant sharp absorption at ~1434-1439 cm^{-1}, and a weaker band at ~868-882 cm^{-1} were observed.

In striking contrast, the relative intensities of all three types of bands (the C-H stretching band, the O-H broad band, and the large (~1434-1439 cm^{-1}) band due to Zn-O stretching vibrations) follows the patter as ZnS exhibits the largest intensity, then ZnN, then ZnK and ZnB exhibits the smallest. The uncapped blank sample retains a significant (~1434 cm^{-1}) band and a moderate C-H/O-H signature when no organic capping agent is present at all, which is consistent with a surface carbonate (from atmospheric CO_2 uptake or precipitation route) contribution rather than a contribution from phytoconstituents. The addition of each capping agent to the surface of ZnO resulted in increasing intensity and width particularly in the O-H region of this baseline carbonate/lattice water contribution by both capping-agent derived hydroxyl groups (phenol/flavone) and adsorbed moisture (Mirzaei & Darroudi, 2017; Morgan & Aboshanab, 2024; Raha & Ahmaruzzaman, 2022). The weaker ~868-882 cm^{-1} band, tentatively assigned to a carbonate out-of-plane bending mode (often observed as a diagnostic pair with the ~1430 cm^{-1} asymmetric stretch) or a Zn-OH bending vibration, did not follow the same clean monotonic trend (ZnK showed the lowest intensity of the four, rather than ZnB), and is accordingly interpreted as a shared structural/surface-hydroxyl feature common to the wurtzite ZnO lattice itself rather than a capping-agent-specific marker. Finally, all four spectra showed a steep rising absorption edge as the recorded range approached its lower limit (~550-600 cm^{-1}), consistent with the onset of the strong Zn-O lattice (phonon) stretching vibration expected in the 400-600 cm^{-1} region for wurtzite ZnO; however, the spectra as recorded do not extend far enough to resolve the actual band minimum, so an exact Zn–O stretching frequency cannot be reported from this measurement.

In all four FTIR spectra (ZnB, ZnK, ZnN, and ZnS), a steep, monotonically descending absorption edge was observed beginning near 550–600 cm^{-1} and continuing to fall sharply toward the lower limit of the recorded range. This feature is characteristic of the onset of the Zn-O lattice stretching vibration, which for hexagonal wurtzite ZnO is typically reported in the 400-600 cm^{-1} region of the infrared spectrum(Gaur et al., 2024).

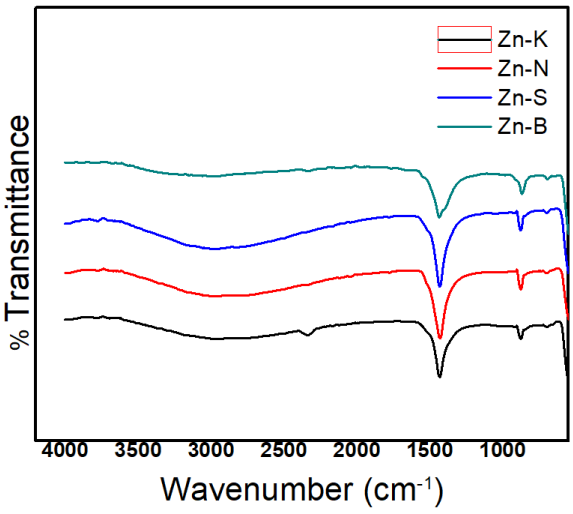


Figure 3: FTIR peaks of the sample ZnB, ZnK, ZnN, ZnS

3.4 BET surface area analysis

The specific surface area of the synthesised ZnO nanoparticles was determined by nitrogen (N_2) adsorption–desorption analysis at 77 K using an automatic surface area analyser (Serial No. 580) with an adsorption cross-sectional area of 0.162 nm² for N_2. Prior to measurement, all samples were degassed at 200°C for 4 hours under vacuum (1.223×10^{-3} Pa) to remove adsorbed moisture and surface contaminants. The BET specific surface area was calculated from the linear region of the BET plot in the relative pressure (P/P_0) range of 0.05–0.30. Nitrogen Adsorption – Desorption Analysis of samples as determined from Table 2 revealed that the Specific Surface Area of the four sample types followed an order of ZnS (6.08 m²/g) > ZnN (4.78 m²/g) > ZnK (4.31 m²/g) > ZnB (3.76 m²/g). The surface energy can be estimated using $Es = \gamma ZnO \times SBET$ (where $\gamma ZnO = 1.0$ J/m²) for each sample based on their BET surface areas listed in the tables.

Table 2: *$Es = \gamma ZnO \times SBET$ ($\gamma ZnO = 1.0$ J/m²) may be used to estimate the surface energy of each sample from the tabulated BET surface areas, following the convention used elsewhere in this work.*

Sample	Capping agent	Sample wt. (g)	BET S.A. (m²/g)	C constant	Vm (cm³ STP/g)	Total pore vol. (cm³/g)	Mean pore dia. (nm)
ZnB	Blank (uncapped)	0.4483	3.7590	120.96	0.8636	0.02319	24.671
ZnK	Cinnamomum verum	0.3818	4.3093	122.31	0.9901	0.03037	28.186
ZnN	Azadirachta indica	0.4684	4.7825	131.43	1.0988	0.02875	24.048
ZnS	Ruta graveolens	0.3733	6.0794	241.26	1.3968	0.03407	22.419

3.5 In vitro cytotoxicity against HeLa cells (MTT assay)

Cytotoxicity of ZnB, ZnK, ZnN, and ZnS toward HeLa (human cervical cancer) cells was evaluated by the MTT assay following 24 h treatment at five concentrations (6.25, 12.5, 25, 50, and 100 µg/mL), with an untreated control set to 100% viability. Each concentration was tested in triplicate; absorbance was read at 540 nm. Cell viability decreased in a clear, statistically significant, dose-dependent manner for all four samples ($p < 0.001$ vs. control at every tested concentration; Table 3, Figure 3).

Table 3. *Percentage viability of HeLa cells following 24 h treatment with (a) ZnB, (b) ZnK, (c) ZnN, and (d) ZnNK at 6.25–100 µg/mL (*** $p < 0.001$ vs. untreated control).*

Concentration (µg/mL)	*ZnB (% viability)*	*ZnK (% viability)*	*ZnN (% viability)*	*ZnS (% viability)*
Control	*100.00*	*100.00*	*100.00*	*100.00*
6.25	93.75	*89.52*	*87.82*	*68.02*
12.5	83.47	*71.09*	*64.36*	*53.43*
25	68.07	*56.27*	*50.44*	*33.12*
50	32.93	*34.57*	*30.50*	*25.72*
100	23.79	*26.37*	*20.25*	*16.19*

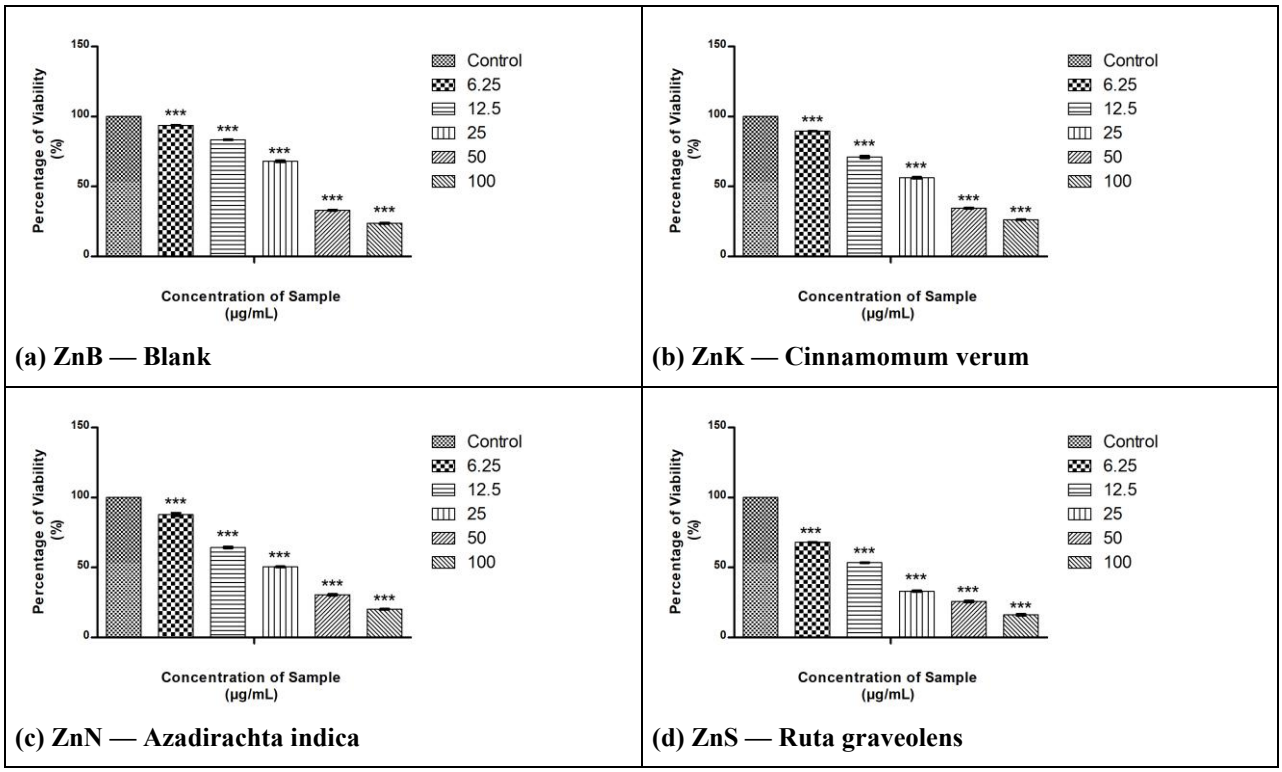
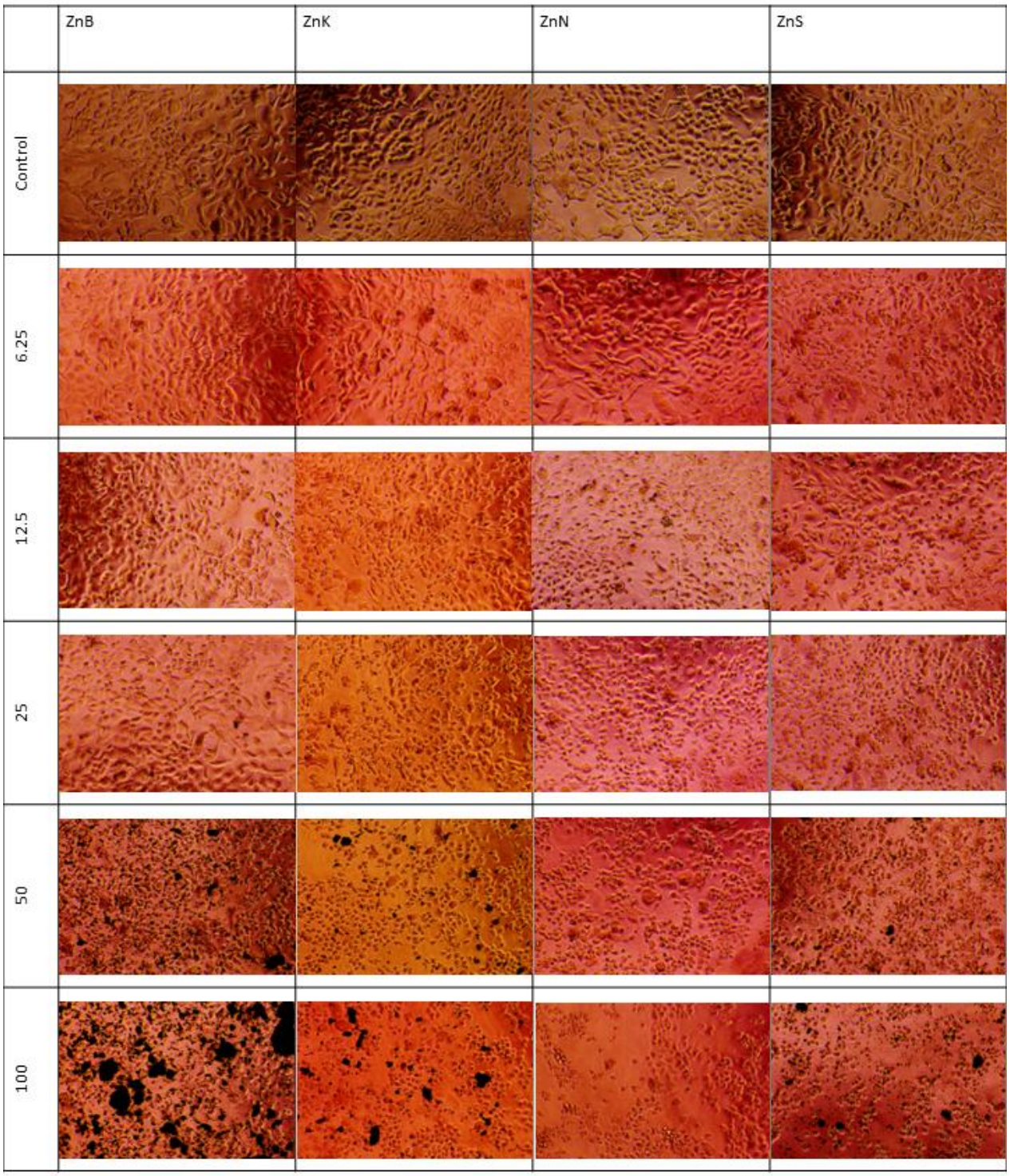


Figure 4. *Percentage viability of HeLa cells following 24 h treatment with (a) ZnB, (b) ZnK, (c) ZnN, and (d) ZnS at 6.25–100 µg/mL (*** $p < 0.001$ vs. untreated control).*

Figure 5. Phase-contrast micrographs of HeLa cells following 24 h treatment with ZnB, ZnK, ZnN, and ZnS at 0 (control), 6.25, 12.5, 25, 50, and 100 µg/mL.



Half-maximal inhibitory concentration (IC50) values, calculated from the dose–response curves using ED50 PLUS v1.0 software, are summarised as, ZnS (IC50 = 25.56µg/mL) > ZnK (IC50 = 32.23µg/mL) > ZnB (IC50 = 37.86µg/mL). A lower IC50 value indicates higher potency(Berrouet et al., 2020). Thus, the Ruta graveolens capped sample (ZnS) is approximately 2.6 - fold more potent than the un-capped blank (ZnB) based on IC50. The other two samples, ZnK and ZnN also exhibited

smaller crystallite size and larger Brunauer-Emmett-Teller surface area (surface area BET) than did the un-capped blank; both were significantly more cytotoxic than the un-capped blank. These results are consistent with a mechanism of action involving the generation of reactive oxygen species (ROS) and/or the intracellular release of free Zn^{2+} ions via the surface area/reaction rate driven process (Shobha et al., 2019; Sportelli et al., 2022), whereby increased specific surface area and/or surface reactivity result in increased production of ROS and increased efficiency of Zn^{2+} ion release after cellular uptake (Lorenzo-Leal et al., 2019; Mongy & Shalaby, 2024).

3.6 Structure–activity correlation (summary)

In bringing all of Sections 3.1-3.5 into a single framework, a coherent and mostly well-coordinated view can be seen throughout the entire group. The sample capped with *Ruta graveolens* (ZnS) contained the least amount of average XRD crystallite size (16.9nm), had the "urchin-like" FESEM morphological features which are unique and have the largest curvature, the greatest BET surface area (6.08m^2/g) and adsorption interaction constant C (241.3), and the smallest (or most potent) HeLa IC50 (14.61µg/mL) of the 4 samples examined each independent measurement indicated a common direction. The sample capped with *Azadirachta indica* (ZnN) exhibited a very similar, but slightly less distinct, trend; small crystallites compared to the blank (18.0 nm avg.), an intermediate BET surface area and a higher than blank cytotoxic effect. Although it exhibited smaller crystallites (25.1 nm avg.) than those of the blank, the BET surface area (3.76 m^2/g) and cytotoxic potency (HeLa IC50=37.86 µg/mL) of the sample capped with *Cinnamomum verum* (ZnK) were lower than those of the blank. This disparity may seem puzzling until viewed through FESEM images (Section 3.2) which clearly show that many of the surfaces of the secondary particles of ZnK are buried due to heavy fusion/ aggregation. Therefore, while nominal crystalline particle size has set an upper limit on available surface area, the extent of aggregation (the degree to which secondary particles fuse together), easily determined by FESEM and quantitatively measured via BET, will determine how much of the available surface area will ultimately be realized and thus made available to the assay medium. Thus, across the ZnB, ZnN and ZnS, BET surface area and cytotoxic potency demonstrated a close tracking relationship to one another and also to the crystalline particle size trends observed. Conversely, ZnK demonstrated a significant departure from these relationships which was completely explainable based upon the morphological differences associated with ZnK versus ZnB, ZnN, and ZnS. Specifically, while ZnK did exhibit an unusual morphology characterized by large aggregates, its crystal structure remained unchanged from that expected based upon X-ray diffraction measurements (wurtzite type crystal structure with normal lattice parameters); therefore, no possible explanations could be attributed to changes in either the phase or strains within the ZnK material. In summary, the surface area/aggregation state and surface reactivity (as evidenced by BET C-constant), rather than solely crystalline particle size and/or capping agent identity, appeared to be responsible for determining the anticancer efficacy in this series. This supports a surface-area driven ROS generation mechanism as proposed for ZnO nanoparticles(Mongy & Shalaby, 2024; Shobha et al., 2019)

4. Conclusion

Blank and *Ruta graveolens*, *Azadirachta indica*, and *Cinnamomum verum* capped ZnO nanoparticles (ZnB, ZnN, ZnK, and ZnS) were made and characterized. XRD indicated a phase pure hexagonal wurzite structure for all four samples. Each sample had peaks that were at the same position and nominal lattice constants ($a \approx 3.24–3.25 A^0$, $c \approx 5.19–5.21 A^0$) indicating that no strain was induced in the lattice during capping. In addition, Scherrer analysis indicated a systematic decrease in crystalline size as the amount of capping agent increased (ZnB, 27.7nm avg.> ZnK, 25.1nm > ZnN, 18.0nm > ZnS, 16.9nm). FESEM images showed that the morphology of each sample varied based upon the capping agent used. For example, the rutacapsule-capped sample formed unique flower/urchin like aggregates while the Kcapsule-capped sample developed large fused granular clusters. The BET surface areas measured for each sample also varied based upon the type of capping agent used. For example, the rutacapsule-capped sample showed a 27% increase in surface area compared to the blank sample along with a very high C constant, indicating a highly reactive surface. On the other hand, the cinnamon-capsule-capped sample exhibited small crystallites but less surface area than the blank sample. However, this appears to be due to significant agglomeration observed using FESEM. The MTT cytotoxicity assay against HeLa cells demonstrated dose dependent cytotoxic activity for each of the samples across the 6.25–100µgmL concentration range. The IC50 values (fitted with ED50 plus) determined from these studies were 14.61µgmL (ZnS), 25.56µgmL (ZnN), 32.23µgmL(ZnB), and 37.86µgmL (ZnK). Thus, the Ruta graveolens capsulated sample was found to have the greatest level of anticancer potential within this set of compounds. This finding can be correlated

with its smallest crystallite size, highest BET surface area, and most reactive surface. Collectively, these four characterization methods present a similar structure-activity relationship where the crystallite size, degree of agglomeration of particles, total available surface area, and ultimately the cytotoxic potency are all related. Furthermore, it seems that the degree of agglomeration rather than either the particle size or capping agent determines how much of a compound's inherent surface reactivity is expressed biologically. Therefore, these results suggest further investigations into biologically capped ZnO nanoparticles and specifically those capped with Rutagrevolens should continue to investigate their potential as candidate selective anticancer agents.

Acknowledgements

The author(s) thank the Department of Chemistry, St. Mary's College, Sulthan Bathery, for providing the research facilities necessary for this work.

References

[1] G. Bisht and S. Rayamajhi, 2016, "ZnO Nanoparticles: A Promising Anticancer Agent," *SAGE Publications Ltd*. doi: 10.5772/63437.

[2] M. E. Davis, Z. Chen, and D. M. Shin, 2008, "Nanoparticle therapeutics: An emerging treatment modality for cancer," *Nature Publishing Group*. doi: 10.1038/nrd2614.

[3] S. Raha and M. Ahmaruzzaman, 2022, "ZnO nanostructured materials and their potential applications: progress, challenges and perspectives," *Royal Society of Chemistry*. doi: 10.1039/d1na00880c.

[4] S. Maher *et al.*, 2023, "Synthesis and Characterization of ZnO Nanoparticles Derived from Biomass (Sisymbrium Irio) and Assessment of Potential Anticancer Activity," *ACS Omega*, vol. 8, no. 18, pp. 15920–15931, doi: 10.1021/acsomega.2c07621.

[5] V. Kaliyaperumal, R. I. Alharbi, H. Rajendhran, D. R. Gopal, and F. O. Al-Otibi, 2024, "Beta-cyclodextrin-Phyllanthus emblica emulsion for zinc oxide nanoparticles: Characteristics and photocatalysis," *Green Processing and Synthesis*, vol. 13, no. 1, doi: 10.1515/gps-2024-0056.

[6] N. D. S. Zambri, N. I. Taib, F. A. Latif, and Z. Mohamed, 2019, "Utilization of neem leaf extract on biosynthesis of iron oxide nanoparticles," *Molecules*, vol. 24, no. 20, doi: 10.3390/molecules24203803.

[7] K. Lingaraju *et al.*,2016, "Biogenic synthesis of zinc oxide nanoparticles using Ruta graveolens (L.) and their antibacterial and antioxidant activities," *Applied Nanoscience (Switzerland)*, vol. 6, no. 5, pp. 703–710, doi: 10.1007/s13204-015-0487-6.

[8] H. Sung *et al.*,2021, "Global Cancer Statistics 2020: GLOBOCAN Estimates of Incidence and Mortality Worldwide for 36 Cancers in 185 Countries," *CA Cancer J. Clin.*, vol. 71, no. 3, pp. 209–249, doi: 10.3322/caac.21660.

[9] C. A. Burmeister *et al.*, 2022, "Cervical cancer therapies: Current challenges and future perspectives," *Elsevier B.V.* doi: 10.1016/j.tvr.2022.200238.

[10] A. Pal and R. Kundu, 2020, "Human Papillomavirus E6 and E7: The Cervical Cancer Hallmarks and Targets for Therapy," *Frontiers Media S.A.* doi: 10.3389/fmicb.2019.03116.

[11] T. dos Santos, J. Varela, I. Lynch, A. Salvati, and K. A. Dawson, 2011, "Effects of transport inhibitors on the cellular uptake of carboxylated polystyrene nanoparticles in different cell lines," *PLoS One*, vol. 6, no. 9, doi: 10.1371/journal.pone.0024438.

[12] Malgorzata. Baranska, 2014, *Optical spectroscopy and computational methods in biology and medicine*. Springer.

[13] S. Anjum *et al.*, 2021, "Recent advances in zinc oxide nanoparticles (Zno nps) for cancer diagnosis, target drug delivery, and treatment," *Cancers (Basel).*, vol. 13, no. 18, doi: 10.3390/cancers13184570.

[14] G. Mani, A. V. Kumar, and S. Mathew, 2023, "ZIF-8 derived ZnO: a facile catalyst for ammonium perchlorate thermal decomposition," *RSC Sustainability*, vol. 1, no. 8, pp. 2081–2091, doi: 10.1039/d3su00256j.

[15] H. Ji *et al.*, 2025, "CuO-ZnO heterojunction for enhanced catalytic decomposition of ammonium perchlorate via interfacial promotion," *J. Alloys Compd.*, vol. 1044, doi: 10.1016/j.jallcom.2025.184539.

[16] H. Mirzaei and M. Darroudi, 2017, "Zinc oxide nanoparticles: Biological synthesis and biomedical applications," *Elsevier Ltd*. doi: 10.1016/j.ceramint.2016.10.051.

[17] R. N. Morgan and K. M. Aboshanab, 2024, "Green biologically synthesized metal nanoparticles: biological applications, optimizations and future prospects," *Taylor and Francis Ltd.* doi: 10.2144/fsoa-2023-0196.

[18] J. Gaur *et al.*, 2024, "CTAB-crafted ZnO nanostructures for environmental remediation and pathogen control," *Sci. Rep.*, vol. 14, no. 1, doi: 10.1038/s41598-024-65783-x.

[19] C. Berrouet, N. Dorilas, K. A. Rejniak, and N. Tuncer, 2020, "Comparison of Drug Inhibitory Effects (IC 50) in Monolayer and Spheroid Cultures," *Bull. Math. Biol.*, vol. 82, no. 6, doi: 10.1007/s11538-020-00746-7.

[20] N. Shobha *et al.*, 2019, "Synthesis and characterization of Zinc oxide nanoparticles utilizing seed source of Ricinus communis and study of its antioxidant, antifungal and anticancer activity," *Materials Science and Engineering C*, vol. 97, pp. 842–850, doi: 10.1016/j.msec.2018.12.023.

[21] M. C. Sportelli *et al.*, 2022, "Biogenic Synthesis of ZnO Nanoparticles and Their Application as Bioactive Agents: A Critical Overview," *Multidisciplinary Digital Publishing Institute (MDPI)*. doi: 10.3390/reactions3030030.

[22] A. C. Lorenzo-Leal, E. Palou, A. López-Malo, and H. Bach, 2019, "Antimicrobial, Cytotoxic, and Anti-Inflammatory Activities of Pimenta dioica and Rosmarinus officinalis Essential Oils," *Biomed Res. Int.*, vol. doi: 10.1155/2019/1639726.

[23] Y. Mongy and T. Shalaby, 2024, "Green synthesis of zinc oxide nanoparticles using Rhus coriaria extract and their anticancer activity against triple-negative breast cancer cells," *Sci. Rep.*, vol. 14, no. 1, doi: 10.1038/s41598-024-63258-7.